PROCEEDINGS OF SCIENCE

$\mu \to e$ conversion in nuclei and nuclear charge distributions[†]

Frederic Noël[a,*] **and Martin Hoferichter**[a]

[a] *Albert Einstein Center for Fundamental Physics, Institute for Theoretical Physics, University of Bern, Sidlerstrasse 5, 3012 Bern, Switzerland*

E-mail: noel@itp.unibe.ch

$\mu \to e$ conversion in nuclei gives one of the leading limits on lepton-flavor-violating (LFV) processes, with upcoming measurements calling for a more consistent theoretical description. This can be done model independently using an effective-field-theory framework in terms of effective beyond-Standard-Model operators, which, however, crucially depends on hadronic and nuclear matrix elements. In particular, the uncertainties inherent in these non-perturbative inputs limit the discriminating power that can be achieved. In order to quantify the associated uncertainties, we revisit nuclear charge densities and propagate uncertainties from elastic electron scattering experiments. These charge densities, parameterized in terms of Fourier–Bessel series, can be correlated with results from modern ab-initio methods and thus allow for the evaluation of general $\mu \to e$ conversion rates with quantified uncertainties. The resulting description of $\mu \to e$ conversion enables improved studies of the appearing effective operators, which can also be related to LFV pseudoscalar decays.

The 11th International Workshop on Chiral Dynamics (CD2024)
26-30 August 2024
Ruhr University Bochum, Germany

[†] The contents of this work are based on Refs. [1–4], see Ref. [5] for related proceedings.
[*] Speaker

 ISSN 1824-8039 . Published by SISSA Medialab.

PoS(CD2024)109

LFV process	current limit	(planned) experiments
$\mu \to e\gamma$	$< 4.2 \times 10^{-13}$ [7]	MEG II [8]
$\mu \to 3e$	$< 1.0 \times 10^{-12}$ [9]	Mu3e [10]
$\tau \to \ell\gamma, 3\ell, \ell P, \ldots$	$\lesssim 10^{-8}$ [11–18]	Belle II [19], ...
$K \to \mu e, \mu e\pi, \mu e\pi\pi$	$\lesssim 10^{-11}$ [20–23]	KOTO [24], LHCb [25]
$\pi^0 \to \mu e$	$< 3.6 \times 10^{-10}$ [22, 23, 26, 27]	JEF [29], REDTOP [30]
$\eta \to \mu e$	$< 6 \times 10^{-6}$ [28]	
$\eta' \to \mu e$	$< 4.7 \times 10^{-4}$ [31]	
Au $\mu^- \to$ Au e^-	$< 7 \times 10^{-13}$ [32]	
Ti $\mu^- \to$ Ti e^-	$< 6.1 \times 10^{-13}$ [33]	
Al $\mu^- \to$ Al e^-	$\lesssim 10^{-17}$ (projected)	Mu2e [34], COMET [35]

Table 1: A selection of LFV processes and limits on their branching ratios given at 90% confidence level. The conversion rate is normalized to the muon capture rate [36].

1. Introduction

Lepton-flavor-violating (LFV) processes are promising observables in the search for physics beyond the Standard Model (BSM), as lepton flavor is an accidental symmetry that may well be violated by BSM extensions, beyond neutral LFV observed via neutrino oscillations [6]. Thus, the consideration of LFV operators in a general effective-field-theory (EFT) manner is a natural SM extension. As the SM conserves lepton flavor (up to tiny corrections induced by neutrino oscillations), any observation would be a direct BSM signal, while improved limits put very stringent bounds on the LFV operators, which results in significant restrictions on potential BSM scenarios. An incomplete selection of current limits on LFV processes is given in Table 1.

On the one hand, the currently most stringent limits come from the purely leptonic channels $\mu \to e\gamma$ and $\mu \to 3e$ with future improvements expected from MEG II [8] and Mu3e [10], respectively. On the other hand, $\mu \to e$ conversion probes complementary effective operators to the leptonic channels and gives similarly stringent limits on LFV, with upcoming substantial experimental improvements at Mu2e [34] and COMET [35] reaching for a precision improvement by up to four orders of magnitudes. The limits for LFV decays of light pseudo-scalars are much less stringent but could see some improvements from the planned eta factory experiments of REDTOP [30] or JEF [29]. Here it has been shown, though, that since they probe the same operators as spin-dependent $\mu \to e$ conversion, the limits on $\mu \to e$ conversion already imply significantly stronger indirect limits on these processes, rendering them less compelling probes of LFV [1], see Sec. 3.

Due to these upcoming experimental advances in $\mu \to e$ conversion, it is timely to develop a comprehensive description of $\mu \to e$ conversion that enables robust, quantitative statements about the effective LFV operators. To describe $\mu \to e$ conversion in a model-independent way starting from the underlying LFV operators, the associated Wilson coefficients, originally defined at the high scale, need to be evolved by a concatenation of different EFTs to the low scale where the experiments

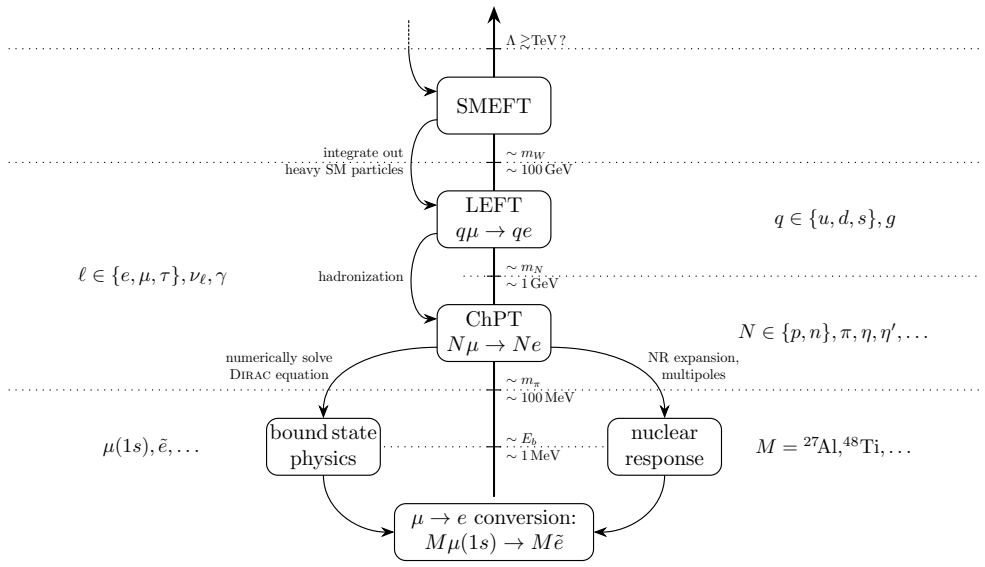

Figure 1: Schematic representation of the EFT scales for $\mu \to e$ conversion.

are performed [1–4, 37–48]. $\mu \to e$ conversion is particularly intricate in this regard due to the many scales involved. After running the effective operators down to the electroweak scale [49–51] and integrating out the heavy SM particles, the effective quark-level operators are turned into hadronic operators using the hadronic matrix elements, which are then, in turn, embedded into nuclear responses employing nuclear matrix elements. Finally, Coulomb corrections on the leptonic side of the interaction need to be considered. The different scales and EFTs relevant for this process are illustrated in Fig. 1. Using this approach and combining all these aspects leads to a comprehensive EFT framework describing $\mu \to e$ conversion. The resulting description will consist of four aspects: the EFT operators, the hadronic matrix elements, the nuclear matrix elements, and the Coulomb corrections, as illustrated in Fig. 2.

All these aspects must be well under control to infer meaningful implications from the experimental limits. For these reasons, controlling uncertainties at all steps along the way is important. While for the majority of the hadronic matrix elements lattice-QCD and/or phenomenological determinations exist, so far, the nuclear matrix elements have been largely based on empirical models such as the nuclear shell model, whose uncertainties are hard to assess especially for quantities for which direct experimental validation is difficult to obtain, most notably, nuclear responses related to neutron distributions. Only recently experimental measurements of parity-violating electron scattering (PVES) have become available, allowing for a test of neutron responses [52–54]. However, these measurements only exist for a few isotopes and typically a single momentum transfer, which does not suffice for an empirical determination of neutron densities. To address these shortcomings, ab-initio nuclear-structure methods can be employed to calculate the nuclear matrix elements, implementing important properties of QCD such as chiral symmetry. In fact, the uncertainties are dominated by the considered chiral Hamiltonians and not by the many-body calculations, which suggests a correlation analysis to relate the neutron responses to their experimentally much better known proton analogs [55, 56]. In these proceedings, we report on the application of this method to provide results for the so-called overlap integrals in $\mu \to e$ conversion, which combine the

Figure 2: Schematic representation of the components of the EFT framework for $\mu \to e$ conversion.

nuclear responses and the Coulomb corrections, based on nuclear charge distributions extracted from elastic electron–nucleus scattering, including quantified uncertainties. At the same time, the nuclear charge distribution also plays an important role in the Coulomb corrections, as it defines the nucleus potential that distorts the muon and electron wave functions.

2. $\mu \to e$ conversion in nuclei

$\mu \to e$ conversion in nuclei refers to the process in which a muon bound to a nucleus in the $1s^{1/2}$ ground state converts into an electron without emitting neutrinos. Since, up to a small recoil of the nucleus, the mass of the muon is converted into kinetic energy of the electron, the electron will then be ejected from the nucleus, while its wave function is distorted by the nucleus potential. On the quark level, this process can happen either via a variety of point interactions with the quarks and gluons in the nucleus or via a long-distance one-photon exchange. The latter one we call the dipole interaction, which is also probed by $\mu \to e\gamma$. The point interactions always occur between two leptons and two of the same quarks or gluons, and thus are not probed at tree level by the leptonic channels. The full Lagrangian relevant for $\mu \to e$ conversion below the electroweak scale up to dimension 7 can be written as

$$\mathcal{L}_{\text{eff}}^{\mu\to e} = \sum_{Y=L,R} \left(\sum_{q=u,d,s} \sum_{\substack{X=S,P,\\ V,A,T}} C_Y^{X,q}\, L_Y^{X,(n)}\, Q_{(n)}^{X,q} + \sum_{\substack{X=D,\\ GG,G\tilde{G}}} C_Y^{X}\, L_Y^{X,(n)}\, Q_{(n)}^{X} + \text{h.c.} \right), \tag{1}$$

with

$$\begin{aligned}
L_Y^S &= \Lambda^{-2}\, \overline{e_Y}\mu, & Q^{S,q} &= \bar{q}q,\\
L_Y^P &= L_Y^S, & Q^{P,q} &= \bar{q}\gamma^5 q,\\
L_Y^{V,\mu} &= \Lambda^{-2}\, \overline{e_Y}\gamma^\mu\mu, & Q_\mu^{V,q} &= \bar{q}\gamma_\mu q,\\
L_Y^{A,\mu} &= L_Y^{V,\mu}, & Q_\mu^{A,q} &= \bar{q}\gamma_\mu\gamma^5 q,\\
L_Y^{T,\mu\nu} &= \Lambda^{-2}\, \overline{e_Y}\sigma^{\mu\nu}\mu, & Q_{\mu\nu}^{T,q} &= \bar{q}\sigma_{\mu\nu}q,\\
L_Y^{GG} &= \Lambda^{-1}\, L_Y^S, & Q^{GG} &= \alpha_s G^a_{\alpha\beta} G_a^{\alpha\beta},\\
L_Y^{G\tilde{G}} &= \Lambda^{-1}\, L_Y^S, & Q^{G\tilde{G}} &= i\alpha_s G^a_{\alpha\beta} \tilde{G}_a^{\alpha\beta},\\
L_Y^{D,\mu\nu} &= \Lambda\, L_Y^{T,\mu\nu}, & Q_{\mu\nu}^{D} &= F_{\mu\nu},
\end{aligned} \tag{2}$$

with the labels referring to scalar (S), pseudo-scalar (P), vector (V), axial-vector (A), tensor (T), dipole (D), and the gluon structure, respectively, and $(n) = \emptyset, \mu, \mu\nu$ is a shorthand for contracting

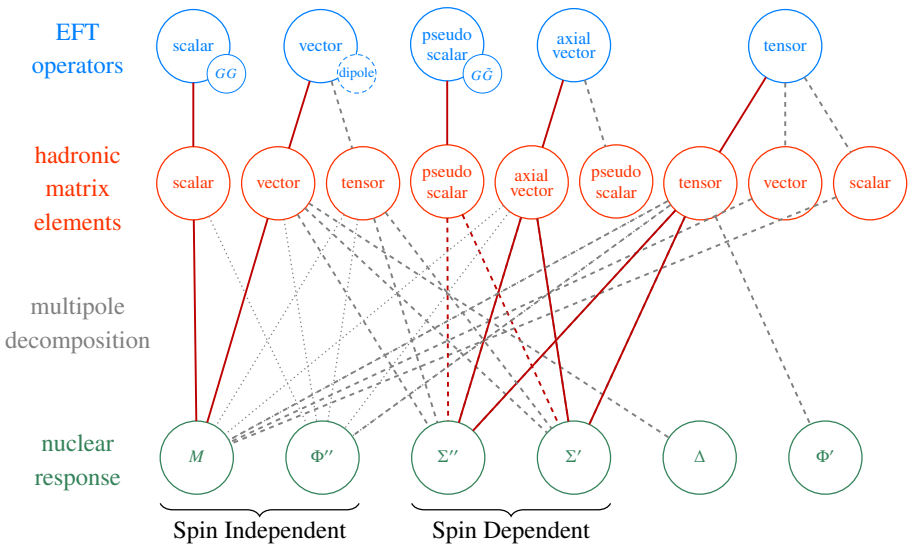

Figure 3: Decomposition of the hadronic side of $\mu \to e$ conversion from the EFT operators to the resulting nuclear responses. Dashed lines are suppressed by q/m_N, dotted lines by q^2/m_N^2.

any kind of Lorentz structure. These quark-level interactions then couple to nucleons via hadronic matrix elements, which finally map onto different nuclear responses via a multipole decomposition. Figure 3 shows how the hadronic part of the different effective operators ultimately contributes to the different nuclear responses, following the procedure of Fig. 1. For a derivation and more detailed version of this illustration, we refer to Ref. [3]. At leading order, one distinguishes between two groups of nuclear responses. The spin-independent (SI) interactions show a coherent enhancement with the number of nucleons in the nucleus, such that the conversion rate scales with the number of nucleons squared $\#N^2$, where $\#N$ is Z for proton responses and $A - Z$ for neutron responses. The spin-dependent (SD) interactions do not show this kind of enhancement as the spins of the nucleons are not all aligned in a nucleus but rather tend to cancel each other out. Thus SD interactions only exist for nuclei with non-zero total nucleus spin and are not coherently enhanced. This also means that experimental limits imply much more stringent constraints on SI than on SD interactions.

In this work, we focus on the SI interactions, whose leading contributions originate from scalar, vector, and dipole operators, as can be deduced from Fig. 3. The resulting SI $\mu \to e$ conversion rate is conventionally expressed in terms of so-called overlap integrals [37], according to

$$\mathrm{Br}^{\mathrm{SI}}_{\mu\to e} = \frac{4m_\mu^5}{\Gamma_{\mathrm{cap}}} \sum_{Y=L,R} \left| \bar{C}_Y^D D + \sum_{N=p,n} \left[\bar{C}_Y^{S^{(N)}} S^{(N)} + \bar{C}_Y^{V^{(N)}} V^{(N)} \right] \right|^2, \tag{3}$$

with the muon capture rate Γ_{cap}. The overlap integrals $S^{(N)}$, $V^{(N)}$, and D combine the inputs from the nuclear responses and the Coulomb corrections, see Sec. 4 for the precise definition. The prefactors are given as a combination of Wilson coefficients and hadronic matrix elements according

to[1]

$$\begin{aligned}
\bar{C}_Y^{S^{(N)}} &= \frac{1}{\Lambda^2}\sum_q C_Y^{S,q}\frac{m_N}{m_q}f_q^N + \frac{4\pi}{\Lambda^3}C_Y^{GG}a_N,\\
\bar{C}_Y^{V^{(N)}} &= \frac{1}{\Lambda^2}\sum_q C_Y^{V,q}F_1^{q,N},\\
\bar{C}_Y^{D} &= \frac{\eta_e}{4m_\mu\Lambda}C_Y^{D},
\end{aligned} \tag{4}$$

where the hadronic matrix elements are defined by

$$\begin{aligned}
\langle N|\, m_q\bar{q}q\,|N\rangle &= \bar{u}'_N\left[m_N f_q^N(q)\right]u_N,\\
\langle N|\,\bar{q}\gamma^\mu q\,|N\rangle &= \bar{u}'_N\left[\gamma^\mu F_1^{q,N}(q) - \frac{i\sigma^{\mu\nu}q_\nu}{2m_N}F_2^{q,N}(q)\right]u_N,\\
\langle N|\, G^a_{\mu\nu}G_a^{\mu\nu}\,|N\rangle &= \bar{u}'_N\left[\frac{4\pi}{\alpha_s}a_N(q)\right]u_N,
\end{aligned} \tag{5}$$

with $\bar{u}_N = \bar{u}_N(p,s)$, $\bar{u}'_N = \bar{u}_N(p',s')$. Here p,s, and p',s' are the momenta and spins of the initial and final nucleon, respectively, and $q = p - p'$, see, e.g., Refs. [1, 58–60] for a review of the required matrix elements. A complete, quantitative description of $\mu \to e$ conversion requires robust input both for the hadronic matrix elements and the overlap integrals, to which we turn in section 4.

3. Pseudo-scalar decays

A similar master formula as Eq. (3) can also be derived for the SD case and for the meson decays $\pi^0, \eta, \eta' \to \mu e$. One then observes that these processes depend on the same set of Wilson coefficients, so that limits on one process imply limits on the other. This connection becomes particularly robust in the case of the π^0, in which case a rigorous limit can be derived when scanning over the entire space of Wilson coefficients, see Fig. 4, orders of magnitude better than the direct limit. For η, η', the general sensitivity also improves by many orders of magnitude over direct limits. In the special case in which only a single Wilson coefficient contributes one finds

$$\mathrm{Br}[\eta \to \mu e] \lesssim 4\times 10^{-12}, \qquad \mathrm{Br}[\eta' \to \mu e] \lesssim 5\times 10^{-13}, \tag{6}$$

but for multiple Wilson coefficients flat directions in parameter space do exist, which may relax these limits. In those cases, however, already RG corrections and the resulting connection to SI limits all but exclude such scenarios.

[1] η_e refers to the sign convention for the charge, corresponding to a minimal coupling of $D_\mu = \partial_\mu + i\eta_e\sqrt{4\pi\alpha_{\rm el}}A^\mu$ [57], $\alpha_{\rm el} = e^2/(4\pi)$.

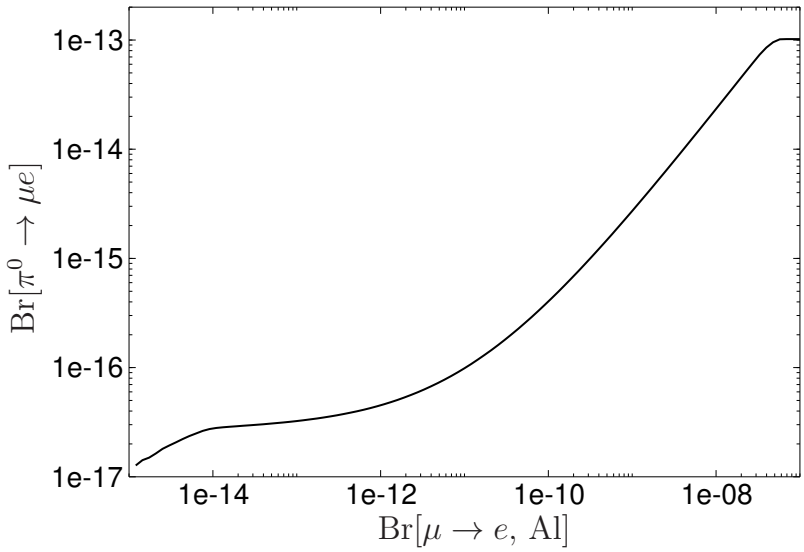

Figure 4: Projection for $\mathrm{Br}[\pi^0 \to \mu e]$ as a function of a future limit for the $\mu \to e$ branching fraction in ^{27}Al and the current limit for ^{48}Ti [33]. In the limit in which the ^{27}Al constraint disappears, one obtains $\mathrm{Br}[\pi^0 \to \mu e] < 1.2 \times 10^{-13}$ [1].

4. Overlap integrals

The overlap integrals combine the nuclear responses with the Coulomb corrections and are given for dipole, scalar, and vector interactions as appearing in Eq. (3) as [37]

$$
\begin{aligned}
D^{(N)} &= -\frac{4}{\sqrt{2}\, m_\mu^{3/2}} \int_0^\infty \mathrm{d}r\, E(r) \left[g^e_{-1}(r)\, f^\mu_{-1}(r) + f^e_{-1}(r)\, g^\mu_{-1}(r) \right], \\
S^{(N)} &= \frac{\#N}{2\sqrt{2}\, m_\mu^{5/2}} \int_0^\infty \mathrm{d}r\, \rho_N(r) \left[g^e_{-1}(r)\, g^\mu_{-1}(r) - f^e_{-1}(r)\, f^\mu_{-1}(r) \right], \\
V^{(N)} &= \frac{\#N}{2\sqrt{2}\, m_\mu^{5/2}} \int_0^\infty \mathrm{d}r\, \rho_N(r) \left[g^e_{-1}(r)\, g^\mu_{-1}(r) + f^e_{-1}(r)\, f^\mu_{-1}(r) \right],
\end{aligned}
\tag{7}
$$

with $N = p, n$ and the electric field given by

$$
E(r) = \frac{\sqrt{4\pi\alpha_{\mathrm{el}}}}{r^2} \int_0^r \mathrm{d}r'\, r'^2 \rho_{\mathrm{ch}}(r'), \tag{8}
$$

in terms of the nuclear charge distribution $\rho_{\mathrm{ch}}(r)$. The weights $\rho_p(r)$ and $\rho_n(r)$ are the point-proton and point-neutron distributions of the nucleus and are directly related to the M multipole responses. In this way, the first factor in the integrals constitutes the nuclear-response contribution to $\mu \to e$ conversion. The latter factor is given by a combination of f^ℓ_κ and g^ℓ_κ with $\ell = e, \mu$, which are the radial parts of the muon and electron wave functions, where the full wave functions are decomposed according to

$$
\psi^\mu_\kappa(\mathbf{r}) = \frac{1}{r} \begin{pmatrix} g_\kappa(r) \phi^\mu_\kappa(\hat{\mathbf{r}}) \\ i f_\kappa(r) \phi^\mu_{-\kappa}(\hat{\mathbf{r}}) \end{pmatrix}, \tag{9}
$$

separating the angular-momentum degrees of freedom into $\phi_\kappa^\mu(\hat{\mathbf{r}})$. The angular-momentum quantum numbers are contained in $\kappa \gtrless 0$ according to

$$j = |\kappa| - \frac{1}{2}, \qquad j_z = \mu, \qquad l = \begin{cases} \kappa & \kappa > 0, \\ -\kappa - 1 & \kappa < 0. \end{cases} \tag{10}$$

These wave functions are found by solving the Dirac equation for the nucleus potential given by the electric field as

$$V(r) = -\sqrt{4\pi\alpha_{\text{el}}} \int_r^\infty \mathrm{d}r'\, E(r'), \tag{11}$$

see Sec. 5 and Refs. [2, 3]. By employing the full solution of the Dirac equation, we automatically incorporate the full Coulomb corrections beyond a plane-wave approximation.

One observes that the charge distribution of the nucleus ρ_{ch} is crucial at several points of the calculation of the overlap integrals. First, the charge distribution defines the electric field according to Eq. (8), which is directly required for the dipole overlap integral D. Second, the electric field defines the nucleus potential used to calculate the muon and electron wave functions. Finally, in Sec. 6 we will show that also improved input for the point-proton and point-neutron distributions can be deduced from the charge distribution using correlations established from ab-initio calculations. Hence, reliable input for the charge distribution, including uncertainty quantification, is crucial for the $\mu \to e$ overlap integrals.

5. Charge distributions

In the previous section, we have shown the importance of precise nuclear charge distributions for the calculation of overlap integrals. In particular, uncertainty estimates for the charge distributions are crucial to assess uncertainties of the overlap integrals. Unfortunately, most of the currently available model-independent parameterizations do not include such uncertainty quantification [61]. For this reason, we revisited the extraction of the charge distributions from electron–nucleus scattering data, to try and propagate the experimental uncertainties and assess the truncation errors when assuming a given parameterization. The differential cross section for $e^-(k) + M(p) \to e^-(k') + M(p')$, the scattering of electrons off a nucleus M, is often written as

$$\frac{\mathrm{d}\sigma}{\mathrm{d}\Omega} = \left(\frac{\mathrm{d}\sigma}{\mathrm{d}\Omega}\right)_{\text{Mott}} \times \frac{E_e'}{E_e} \times \left|F(q,\theta)\right|^2, \tag{12}$$

with momentum transfer $\bar{q}_\mu = k'_\mu - k_\mu = p_\mu - p'_\mu$ and $q = |\mathbf{q}|$. In the plane-wave Born approximation (PWBA), the form factor can be further decomposed into longitudinal, $F_L(q)$, and transverse, $F_T(q)$, components

$$\left|F(q,\theta)\right|^2 = \left|F_L(q)\right|^2 + \left(\frac{1}{2} + \tan^2\frac{\theta}{2}\right)\left|F_T(q)\right|^2, \tag{13}$$

both of which can be further expanded into pieces with definite angular momentum L

$$\left|F_L(q)\right|^2 = \sum_{L\,\text{even}\,\leq 2J} \left|ZF_L^{\text{ch}}(q)\right|^2, \qquad \left|F_T(q)\right|^2 = \sum_{L\,\text{odd}\,\leq 2J} \left|F_L^{\text{mag}}(q)\right|^2, \tag{14}$$

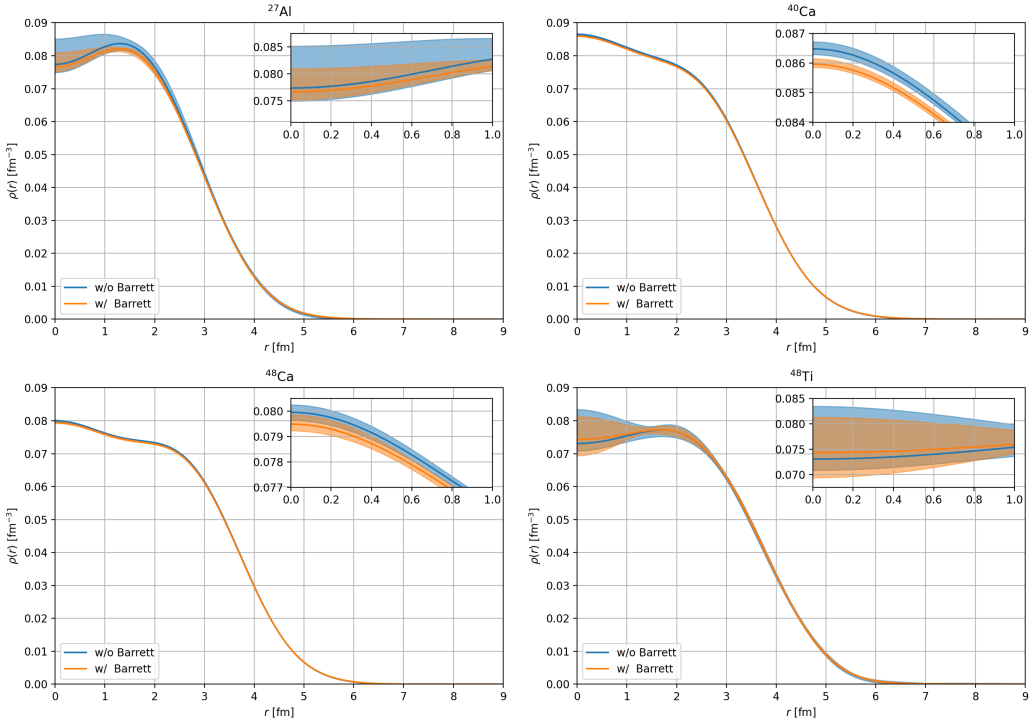

Figure 5: Charge densities of ^{27}Al, ^{40,48}Ca, and ^{48}Ti. Two variants are shown, with (orange) or without (blue) the constraints from Barrett moments [62] as determined from muonic atom spectroscopy [63–66].

where J is the spin of the nucleus. The sole contribution for $J = 0$, and leading contribution in general, is the charge form factor F_0^{ch}. It is directly related to the nuclear charge distribution ρ_{ch} via the Fourier transformation

$$ZF_0^{\text{ch}}(q) = \int \mathrm{d}^3 r\ \rho(r) e^{-i\mathbf{q}\cdot\mathbf{r}} = 4\pi \int \mathrm{d}r\ r^2\, j_0(qr)\rho_{\text{ch}}(r). \tag{15}$$

Hence, if the PWBA were exact and potential higher L contributions under control, the charge distribution would be straightforward to extract from the charge form factor. Unfortunately, even for nuclei with $J = 0$, this extraction becomes complicated by Coulomb corrections. While the PWBA assumes a point-like nucleus with no extension and plane waves for the initial and final electron wave functions, in reality, the extension of the nucleus plays a key role and its potential distorts the electron wave functions. This shifts the cross section and fills out minima in the form factor, which is crucial for an accurate description of the experimental cross-section data.

To include these effects, one again solves the Dirac equation for the electron in the nucleus potential. For $L = 0$ the cross section can then be calculated using the so-called phase-shift model, which uses the asymptotic phase shift differences (compared to the point-like Coulomb problem) for the numerical solutions of the Dirac equation for the different partial waves. An efficient numerical implementation and optimization of the phase-shift model becomes important especially for the estimation of systematic effects, which requires evaluating fits many times over a large space of external parameters. For this reason, we developed the Python package `phasr`, which efficiently performs the procedure of the phase-shift model [67]. Using this package we

were able to extract charge distribution parameterizations for ^{27}Al, ^{40,48}Ca, and ^{48,50}Ti including comprehensive uncertainty estimates containing statistic and systematic components [2], based on the experimental cross section measurements and truncation uncertainties of the expansion into Fourier–Bessel series [68]

$$\rho_{\mathrm{ch}}(r) = \begin{cases} \sum_{n=1}^{N} a_n \, j_0(q_n r) & , \, r \le R \\ 0 & , \, r > R \end{cases} \quad \text{with} \quad q_n = \frac{n\pi}{R} \quad \text{and} \quad j_0(q_n R) = 0. \tag{16}$$

Such a parameterization allows one to represent the charge distribution and derived quantities in a largely model-independent form, as long as the sensitivity to the truncation in N and the cutoff radius R is appropriately taken into account. We show some of the resulting distributions in Fig. 5. For more details on how these distributions were extracted and their uncertainties assessed, we refer to Refs. [2, 3]. Python implementations of these parameterizations including their uncertainty bands are also made available in a Python notebook as supplemental material of Ref. [2].

6. Correlation analysis of overlap integrals

As shown in Eq. (7), in contrast to the dipole overlap integral, the scalar and vector overlap integrals depend on the point-proton and point-neutron distributions. These are not as straightforward to access experimentally as the charge distribution. While the point-proton distribution is the dominating contribution to the charge density, so that only corrections need to be supplemented by nuclear-structure calculations, the neutron density is much harder to probe directly in experiment. Information on the neutron distribution can be determined using PVES or neutrino scattering [69, 70], but, at present, only a very limited amount of data is available that does not suffice to extract the neutron responses from experiment.

For this reason, one needs to employ theoretical calculations for these responses. While phenomenological models often employ approximations that need to be validated by data, current ab-initio calculations, in principle, allow one to predict the responses from few-nucleon input using chiral EFT. In practice, results can still display considerable uncertainties related to EFT truncations and scheme dependence of the chiral Hamiltonian. However, as observed before [55, 56], in many cases, the correlation between the neutron responses and experimental observables, such as the charge radius, proves much more robust than the chiral prediction of the neutron responses themselves, which makes it possible to improve the calculation via such a correlation analysis. This strategy also applies directly to the overlap integrals that depend on point-proton and point-neutron densities, see Sec. 5 and Ref. [2], for which we could establish correlations using a wide range of chiral schemes and orders, see Fig. 6. The many-body calculations are performed using the (valence-space) in-medium similarity renormalization group, (VS-)IMSRG [71–75], with chiral interactions from Refs. [76–80].

In Fig. 6, we consider the isotopes ^{27}Al and ^{48}Ti due to their relevance for $\mu \to e$ conversion, as well as ^{48}Ca as an important benchmark for nuclear-structure calculations with direct application to PVES. The figure shows the correlations between the scalar and vector overlap integrals and the charge radius squared, which are all well described by a simple linear regression. It also lists the resulting values for the overlap integrals. We estimate the fit uncertainty from the distribution of

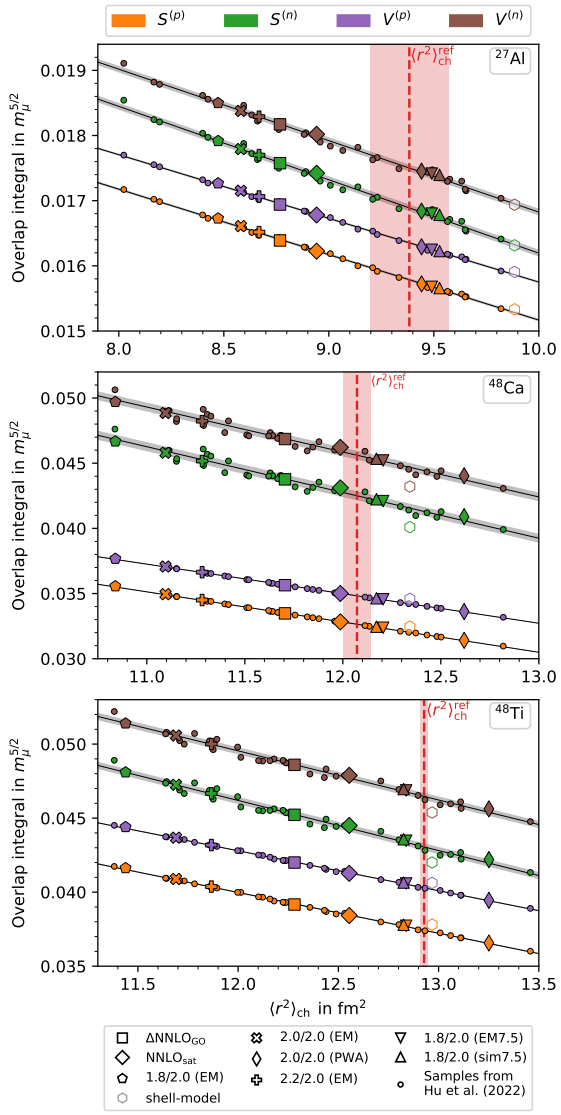

	I_i	This work/[2, 4]	[37]
^{27}Al	D	0.0359(2)	0.0362
	$S^{(p)}$	0.01579(2)(19)	0.0155
	$S^{(n)}$	0.01689(5)(21)	0.0167
	$V^{(p)}$	0.01635(2)(18)	0.0161
	$V^{(n)}$	0.01750(5)(21)	0.0173
^{48}Ca	D	0.07479(10)	–
	$S^{(p)}$	0.03265(03)(16)	–
	$S^{(n)}$	0.04250(34)(25)	–
	$V^{(p)}$	0.03483(02)(16)	–
	$V^{(n)}$	0.04561(34)(24)	–
^{48}Ti	D	0.08640(11)	0.0864
	$S^{(p)}$	0.03742(05)(5)	0.0368
	$S^{(n)}$	0.04305(25)(6)	0.0435
	$V^{(p)}$	0.04029(04)(5)	0.0396
	$V^{(n)}$	0.04646(24)(5)	0.0468

Figure 6: Left: Correlations between the charge radius squared, $\langle r^2 \rangle_{ch}$, and the overlap integrals as defined in Eq. (7), using the IMSRG (specifically VS-IMSRG for ^{27}Al, ^{48}Ti) based on a representative set of chiral Hamiltonians. Right: Resulting overlap integrals. The values for the dipole overlap integral D are reproduced from Ref. [2], with the therein quoted total uncertainty. The other overlap integrals are taken from Ref. [4], where the first uncertainty component quantifies the remaining nuclear-structure uncertainties based on the correlation, and the second one is propagated from the reference value of $\langle r^2 \rangle_{ch}$ [2].

the fit residuals and propagate correlations among the resulting overlap integrals from the residual distributions of the different fits. As a second uncertainty component, we propagate the uncertainties and correlations coming from the reference charge radius squared. For more details on the procedure of the correlation and the assessment of the uncertainties, we refer to Ref. [4].

7. Conclusions

For a systematic study of LFV operators from $\mu \to e$ conversion, controlling uncertainties for all contributions to the conversion rate is crucial. In particular, the accuracy of nuclear responses is hard to quantify, and Coulomb corrections further complicate the situation. We have shown that reliable uncertainty estimates for nuclear charge distributions play an important role in tackling these problems, summarizing the results of Ref. [2], in which we revisited their determination from electron–nucleus scattering. These charge distributions could then be used to calculate the overlap integrals for $\mu \to e$ conversion including uncertainty estimates. For the dipole operator, the transition is immediate, while for the scalar and vector overlap integrals a correlation analysis is required that relates proton and, especially, neutron densities to the charge radius, as established from ab-initio calculation in the (VS-)IMSRG [4]. These overlap integrals constitute the main result of this work, combining the nuclear responses and Coulomb corrections necessary for a systematic study of the SI $\mu \to e$ conversion rate. The generalization to SD responses is in progress.

Acknowledgments

We would like to thank Javier Menéndez for providing shell-model calculations and collaboration on Ref. [1], as well as Matthias Heinz, Takayuki Miyagi, and Achim Schwenk for ab-initio calculations using the (VS-)IMSRG and collaboration on Ref. [4]. Financial support by the SNSF (Project No. TMCG-2_213690) is gratefully acknowledged.

References

[1] M. Hoferichter, J. Menéndez, and F. Noël, Phys. Rev. Lett. **130**, 131902 (2023).

[2] F. Noël and M. Hoferichter, J. High Energy Phys. **08**, 052 (2024).

[3] F. Noël, *$\mu \to e$ conversion in nuclei: EFT description, charge densities, and pseudo-scalar decays*, Ph.D. thesis, Bern U. (2024).

[4] M. Heinz, M. Hoferichter, T. Miyagi, F. Nöel, and A. Schwenk, (2024), arXiv:2412.04545 [nucl-th].

[5] M. Hoferichter and F. Noël, PoS **QCHSC24**, 177 (2025).

[6] Y. Fukuda *et al.* (Super-Kamiokande), Phys. Rev. Lett. **81**, 1562 (1998).

[7] A. M. Baldini *et al.* (MEG), Eur. Phys. J. C **76**, 434 (2016).

[8] A. M. Baldini *et al.* (MEG II), Eur. Phys. J. C **78**, 380 (2018).

[9] U. Bellgardt *et al.* (SINDRUM), Nucl. Phys. B **299**, 1 (1988).

[10] K. Arndt *et al.* (Mu3e), Nucl. Instrum. Meth. A **1014**, 165679 (2021).

[11] B. Aubert *et al.* (BaBar), Phys. Rev. Lett. **98**, 061803 (2007).

[12] Y. Miyazaki *et al.* (Belle), Phys. Lett. B **648**, 341 (2007).

[13] B. Aubert *et al.* (BaBar), Phys. Rev. Lett. **104**, 021802 (2010).

[14] K. Hayasaka *et al.*, Phys. Lett. B **687**, 139 (2010).

[15] Y. Miyazaki *et al.* (Belle), Phys. Lett. B **692**, 4 (2010).

[16] Y. Miyazaki *et al.* (Belle), Phys. Lett. B **719**, 346 (2013).

[17] A. Abdesselam *et al.* (Belle), J. High Energy Phys. **10**, 19 (2021).

[18] N. Tsuzuki *et al.* (Belle), J. High Energy Phys. **06**, 118 (2023).

[19] W. Altmannshofer *et al.* (Belle-II), PTEP **2019**, 123C01 (2019), [Erratum: PTEP **2020**, 029201 (2020)].

[20] D. Ambrose *et al.* (BNL), Phys. Rev. Lett. **81**, 5734 (1998).

[21] A. Sher *et al.*, Phys. Rev. D **72**, 012005 (2005).

[22] E. Abouzaid *et al.* (KTeV), Phys. Rev. Lett. **100**, 131803 (2008).

[23] E. Cortina Gil *et al.* (NA62), Phys. Rev. Lett. **127**, 131802 (2021).

[24] K. Aoki *et al.*, (2021), arXiv:2110.04462 [nucl-ex].

[25] G. Anzivino *et al.*, Eur. Phys. J. C **84**, 377 (2024).

[26] R. Appel *et al.*, Phys. Rev. Lett. **85**, 2450 (2000).

[27] R. Appel *et al.*, Phys. Rev. Lett. **85**, 2877 (2000).

[28] D. B. White *et al.*, Phys. Rev. D **53**, 6658 (1996).

[29] L. Gan *et al.*, "Eta Decays with Emphasis on Rare Neutral Modes: The JLab Eta Factory (JEF) Experiment, JLab proposal," https://www.jlab.org/exp_prog/proposals/14/PR12-14-004.pdf.

[30] J. Elam *et al.* (REDTOP), (2022), arXiv:2203.07651.

[31] R. A. Briere *et al.* (CLEO), Phys. Rev. Lett. **84**, 26 (2000).

[32] W. H. Bertl *et al.* (SINDRUM II), Eur. Phys. J. C **47**, 337 (2006).

[33] P. Wintz, Conf. Proc. C **980420**, 534 (1998).

[34] L. Bartoszek *et al.* (Mu2e), *Mu2e Technical Design Report*, Tech. Rep. (2014) arXiv:1501.05241.

[35] R. Abramishvili *et al.* (COMET), Prog. Theor. Exp. Phys. **2020**, 033C01 (2020).

[36] T. Suzuki, D. F. Measday, and J. P. Roalsvig, Phys. Rev. C **35**, 2212 (1987).

[37] R. Kitano, M. Koike, and Y. Okada, Phys. Rev. D **66**, 096002 (2002), [Erratum: Phys. Rev. D **76**, 059902 (2007)].

[38] V. Cirigliano, R. Kitano, Y. Okada, and P. Tuzon, Phys. Rev. D **80**, 013002 (2009).

[39] A. A. Petrov and D. V. Zhuridov, Phys. Rev. D **89**, 033005 (2014).

[40] A. Crivellin, S. Najjari, and J. Rosiek, J. High Energy Phys. **04**, 167 (2014).

[41] A. Crivellin, M. Hoferichter, and M. Procura, Phys. Rev. D **89**, 093024 (2014).

[42] S. Davidson, Y. Kuno, and M. Yamanaka, Phys. Lett. B **790**, 380 (2019).

[43] E. Rule, W. C. Haxton, and K. McElvain, Phys. Rev. Lett. **130**, 131901 (2023).

[44] V. Cirigliano, K. Fuyuto, M. J. Ramsey-Musolf, and E. Rule, Phys. Rev. C **105**, 055504 (2022).

[45] W. C. Haxton, E. Rule, K. McElvain, and M. J. Ramsey-Musolf, Phys. Rev. C **107**, 035504 (2023).

[46] L. Borrel, D. G. Hitlin, and S. Middleton, arXiv:2401.15025.

[47] W. Haxton, K. McElvain, T. Menzo, E. Rule, and J. Zupan, J. High Energy Phys. **11**, 076 (2024).

[48] F. Delzanno, K. Fuyuto, S. Gonzàlez-Solís, and E. Mereghetti, (2024), arXiv:2411.13497 [hep-ph].

[49] A. Crivellin, S. Davidson, G. M. Pruna, and A. Signer, J. High Energy Phys. **05**, 117 (2017).

[50] V. Cirigliano, S. Davidson, and Y. Kuno, Phys. Lett. B **771**, 242 (2017).

[51] S. Davidson, Y. Kuno, and A. Saporta, Eur. Phys. J. C **78**, 109 (2018).

[52] D. Adhikari *et al.* (PREX), Phys. Rev. Lett. **126**, 172502 (2021).

[53] D. Androić *et al.* (Q_{weak}), Phys. Rev. Lett. **128**, 132501 (2022).

[54] D. Adhikari *et al.* (CREX), Phys. Rev. Lett. **129**, 042501 (2022).

[55] G. Hagen *et al.*, Nat. Phys. **12**, 186 (2015).

[56] C. G. Payne, S. Bacca, G. Hagen, W. G. Jiang, and T. Papenbrock, Phys. Rev. C **100**, 061304 (2019).

[57] J. C. Romao and J. P. Silva, Int. J. Mod. Phys. A **27**, 1230025 (2012).

[58] M. Hoferichter, J. Menéndez, and A. Schwenk, Phys. Rev. D **102**, 074018 (2020).

[59] M. Hoferichter, P. Klos, J. Menéndez, and A. Schwenk, Phys. Rev. D **99**, 055031 (2019).

[60] M. Hoferichter, P. Klos, J. Menéndez, and A. Schwenk, Phys. Rev. D **94**, 063505 (2016).

[61] H. de Vries, C. W. de Jager, and C. de Vries, Atom. Data Nucl. Data Tabl. **36**, 495 (1987).

[62] R. C. Barrett, Phys. Lett. B **33**, 388 (1970).

[63] G. Fricke, C. Bernhardt, K. Heilig, L. A. Schaller, L. Schellenberg, E. B. Shera, and C. W. de Jager, Atom. Data Nucl. Data Tabl. **60**, 177 (1995).

[64] G. Fricke, J. Herberz, T. Hennemann, G. Mallot, L. A. Schaller, L. Schellenberg, C. Piller, and R. Jacot-Guillarmod, Phys. Rev. C **45**, 80 (1992).

[65] H. D. Wohlfahrt, E. B. Shera, M. V. Hoehn, Y. Yamazaki, and R. M. Steffen, Phys. Rev. C **23**, 533 (1981).

[66] G. A. Rinker and J. Speth, Nucl. Phys. A **306**, 397 (1978).

[67] F. Noël, "phasr," (2025).

[68] B. Dreher, J. Friedrich, K. Merle, H. Rothhaas, and G. Lührs, Nucl. Phys. A **235**, 219 (1974).

[69] M. Abdullah *et al.*, (2022), arXiv:2203.07361 [hep-ph].

[70] L. A. Ruso *et al.*, (2022), arXiv:2203.09030 [hep-ph].

[71] H. Hergert, S. K. Bogner, T. D. Morris, A. Schwenk, and K. Tsukiyama, Phys. Rep. **621**, 165 (2016).

[72] S. R. Stroberg, A. Calci, H. Hergert, J. D. Holt, S. K. Bogner, R. Roth, and A. Schwenk, Phys. Rev. Lett. **118**, 032502 (2017).

[73] S. R. Stroberg, S. K. Bogner, H. Hergert, and J. D. Holt, Ann. Rev. Nucl. Part. Sci. **69**, 307 (2019).

[74] H. Hergert, Front. Phys. **8**, 379 (2020).

[75] M. Heinz, T. Miyagi, S. R. Stroberg, A. Tichai, K. Hebeler, and A. Schwenk, arXiv:2411.16014.

[76] K. Hebeler, S. K. Bogner, R. J. Furnstahl, A. Nogga, and A. Schwenk, Phys. Rev. C **83**, 031301 (2011).

[77] A. Ekström, B. D. Carlsson, K. A. Wendt, C. Forssén, M. Hjorth-Jensen, R. Machleidt, and S. M. Wild, J. Phys. G **42**, 034003 (2015).

[78] W. G. Jiang, A. Ekström, C. Forssén, G. Hagen, G. R. Jansen, and T. Papenbrock, Phys. Rev. C **102**, 054301 (2020).

[79] B. S. Hu *et al.*, Nat. Phys. **18**, 1196 (2022).

[80] P. Arthuis, K. Hebeler, and A. Schwenk, (2024), arXiv:2401.06675 [nucl-th].